



Spatiotemporal changes of urban heat island effect relative to land surface temperature: a case study of Jinan City, China

Guiquan Mo¹ · Libo Yan² · Zhiyong Li¹ · Zongyao Wang^{1,3} · Sixuan Chen¹ · Huixuan Li⁴ · Shuwei Zheng¹ · Yurong Cui¹

Received: 12 November 2023 / Accepted: 1 August 2024 / Published online: 12 August 2024
© The Author(s), under exclusive licence to Springer-Verlag GmbH Germany, part of Springer Nature 2024

Abstract

The urban heat island (UHI) effect has become increasingly prevalent and significant with the accelerated pace of urbanization, posing challenges for urban planners and policymakers. To reveal the spatiotemporal variations of the urban heat island effect in Jinan City, this study utilized Landsat satellite images from 2009, 2014, and 2019, employing the classic Mono-Window algorithm to extract land surface temperature (LST). Additionally, Geodetector was introduced to conduct a detailed analysis of the relationship between LST in Jinan City and land cover types (vegetation, water bodies, and buildings). The results indicate a significant increase in the severity of the urban heat island effect in Jinan from 2009 to 2019, with the central urban area consistently exhibiting a high-intensity core heat island. Suburban areas of Jinan show a clear trend of merging their heat island effects with the central urban area. The combined area of strong cool island effect zones and cool island effect zones within water bodies reaches 89.7%, while the combined proportion of heat island and strong heat island effect zones in building areas is 62.2%. Vegetation cover (FVC) exerts the greatest influence among all factors on the intensity level of the urban heat island effect. These findings provide a reliable basis for decision-making related to urban planning and construction in Jinan City.

Keywords Urban heat island · Land surface temperature · Mono-window algorithm · Landsat

Introduction

The urban heat island (UHI) effect has intensified with the expansion of urban areas and the increase in urban population density (Zaitunah et al. 2022), leading to significant

“urban ailments” (Kim and Brown 2021). Examining the influence of different types of land cover on UHI is crucial to deepen our understanding of its formation mechanisms, improve our knowledge of the urban thermal environment, and provide practical guidance for mitigating the UHI effect caused by urbanization.

Responsible Editor: Philippe Garrigues

✉ Yurong Cui
cuiyurong88@126.com

Guiquan Mo
1652960198@qq.com

Libo Yan
852081700@qq.com

Zhiyong Li
3154219756@qq.com

Zongyao Wang
wangzyuka@163.com

Sixuan Chen
1623916668@qq.com

Huixuan Li
huixuan@email.sc.edu

Shuwei Zheng
618067@sdu.edu.cn

¹ College of Geography and Environment, Shandong Normal University, Jinan 250358, China

² Jinan Geotechnical Investigation and Surveying Research Institute, Jinan 250101, China

³ College of Resource Environment and Tourism, Capital Normal University, Beijing 100048, China

⁴ Arnold School of Public Health, University of South Carolina, Columbia, SC 29208, USA

With the rapid growth of remote sensing satellites and related technologies in recent decades, research on the urban heat island (UHI) effect has increasingly focused on its spatial–temporal evolution, influencing factors, simulations, and mechanisms (Liang et al. 2022; Qiao et al. 2019). Common methods for inverting land surface temperature (LST) from remote sensing data include the mono-window algorithm (Qin et al. 2001), radiative balance models (Wan 2014), thermal-emissivity relationship models (Yamamoto and Ishikawa 2018), and combined methods using physical models and inversion algorithms (Kustas and Anderson 2009). Radiative balance models require accurate atmospheric parameters and are computationally complex (Ding et al. 2023), while thermal-emissivity relationship models' accuracy affects inversion precision (Ru et al. 2023). Combined methods involve more data and algorithms, increasing computational complexity (Zhou et al. 2018). This study adopts the mono-window algorithm for its speed, adaptability, and low data requirements. It uses a single thermal infrared band to estimate LST based on thermal radiation principles, atmospheric radiation transmission models, and surface characteristics.

Jinan, the capital city of Shandong Province, is a significant urban center in the Shandong Peninsula City Cluster and the Lower Yellow River City Cluster (Wang et al. 2023). The city's efforts to become a national central city have accelerated its urbanization, further spurred by the merger with Laiwu, Jiyang, and Zhangqiu. These changes have impacted Jinan's thermal environment and the central and western regions of Shandong. Therefore, Jinan is chosen as the research area for this study.

The main objective is to analyze the spatiotemporal characteristics and influencing factors of the UHI effect in Jinan from 2009 to 2019 using LST data from Landsat remote sensing. This analysis aims to support rational urban planning, enhance urban living conditions, and promote environmental protection and ecological construction.

Materials and methods

Study area

The geographical location of Jinan City is in the central part of Shandong Province, with latitude and longitude ranging from 36°02' to 37°54' and 116°21' to 117°93' shown in Fig. 1. The Yellow River is part of the natural boundary to the west of Jinan and flows through the central and northern parts of Jinan. In general, the topography slopes steeper in the south and lower in the north. Jinan's climate is warm temperate continental monsoon, with an average annual precipitation of 548.7 mm. The four seasons are distinct throughout the year with sufficient

sunshine. The rivers in Jinan are part of two main water systems: the Yellow River and the Xiaoqing River. There are also numerous lakes and large reservoirs. The forest vegetation is mainly distributed with trees and shrubs.

Data sources

In this paper, Landsat series satellites were chosen as the remote sensing data. The source was the USGS Earth Explorer website (<https://earthexplorer.usgs.gov>). The vector data used in this study included the prefecture-level and county-level administrative boundary vector files of Jinan City. The data was obtained from the Resource and Environmental Science and Data Center of the Chinese Academy of Sciences (<http://www.resdc.cn>). Land cover classification data comes from the annual land cover classification data of China (Yang, J. and Huang, X., 2021). The DEM data is provided by the Geospatial Data Cloud (<https://www.gscloud.cn/>) as GDEM V2 data. The precipitation data comes from the National Tibetan Plateau Data Center (Peng, S., 2020). In addition, the vector files of Jinan's road network, railways, buildings, water bodies, etc. were obtained from OpenStreetMap which is an open-source map data project. The flow chart of this study is shown in Fig. 2.

Methods

Mono-window algorithm for LST estimation

Its main idea of the mono-window algorithm is to estimate the LST by calculating the thermal energy balance equation using the thermal infrared band (Band 10: 10.60–11.19 μm). The equation is as follows (Eq. (1)):

$$ST = [a(1 - C - D) + [b(1 - C - D) + C + D] \times T - D \times T_a] / C \quad (1)$$

where

$$C = \varepsilon \tau \quad (2)$$

$$D = (1 - \tau)[1 + (1 - \varepsilon)\tau] \quad (3)$$

LST is the land surface temperature; *a* and *b* are the regression coefficients. When the temperature on the surface was between 0° and 70°, *a* and *b* are −67.3554 and 0.4586, respectively. *T* is the brightness temperature. *T_a* is the atmospheric average action temperature. ε is the surface-specific emissivity. τ is the atmosphere transmittance. *LST*, *T*, and *T_a* are in the Kelvin temperature.

According to Eq. (1), atmospheric transmittance τ , atmospheric average action temperature *T_a*, surface

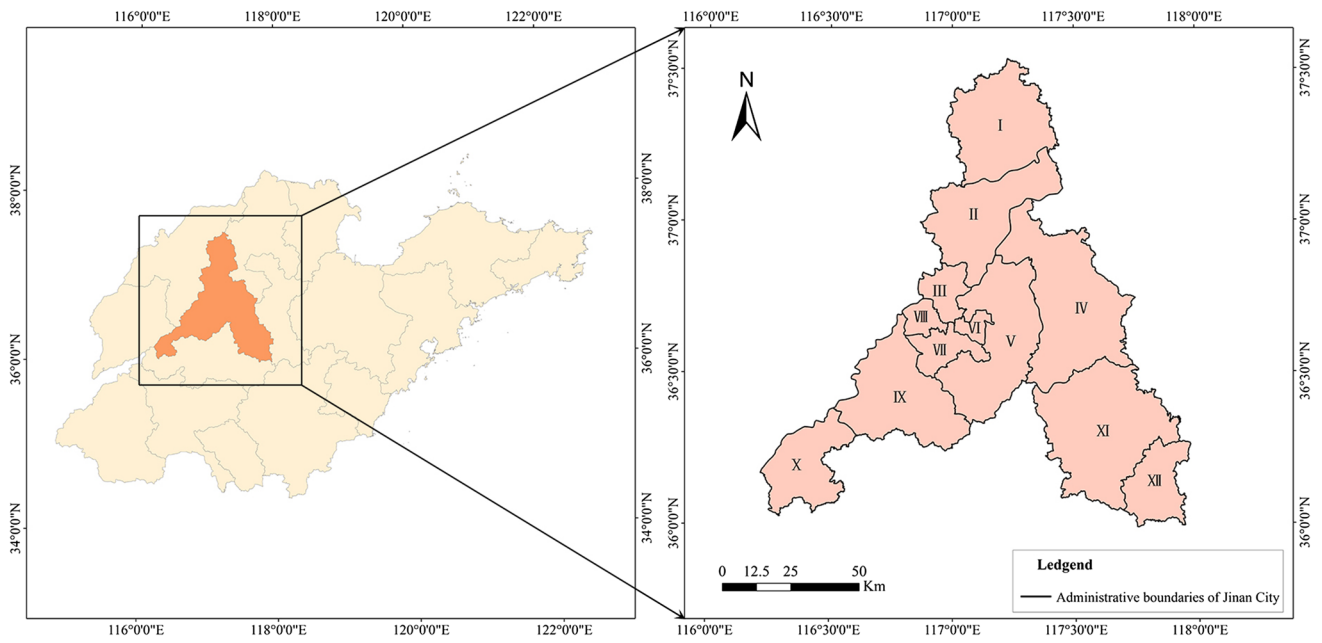


Fig. 1 The administrative divisions of Shandong Province (left); geographical location and administrative division of Jinan (right) (Urban: III, Tianqiao District; V, Licheng District; VI, Lixia District; VII, Central District; VIII, Huaiyin District; Suburban: I, Shanghe

County; II, Jiyang District; IV, Zhangqiu District; IX, Changqing District; X, Pingyin County; XI, Laiwu District; XII, Gangcheng District)

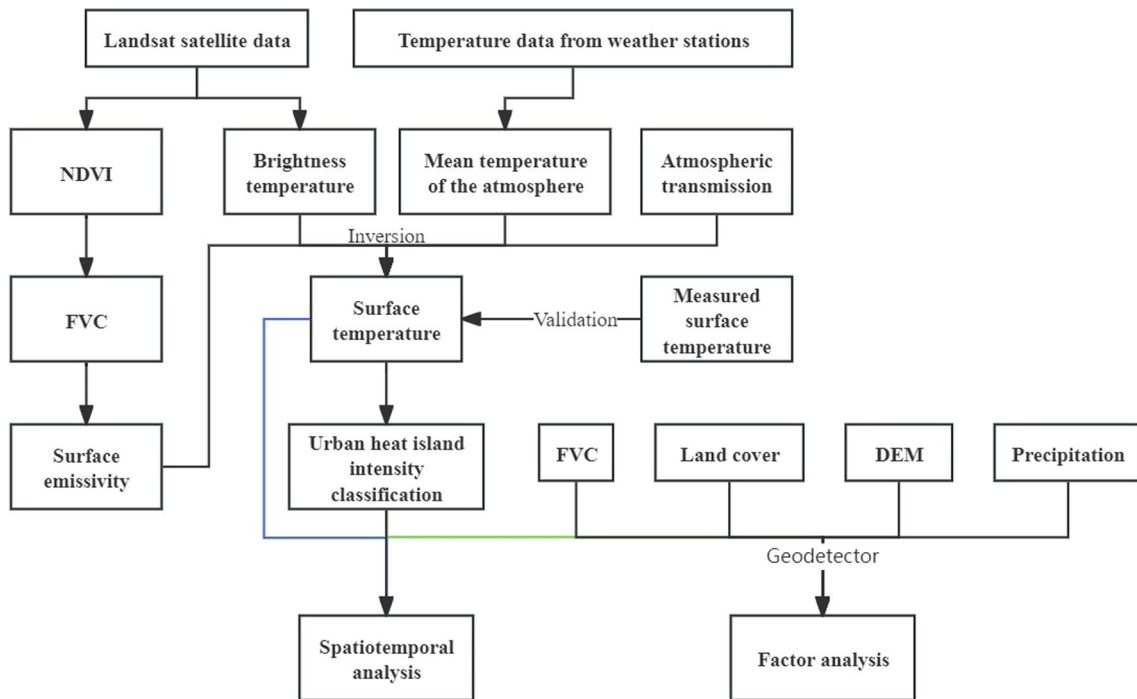


Fig. 2 The flowchart of this study

specific emissivity ϵ , and brightness temperature T are needed to invert the surface temperature. The calculation of these four parameters is shown below.

Atmospheric transmittance τ

The ratio of radiation intensity before and after passing through the atmosphere is referred to as atmospheric transmittance. By entering parameters such as the imaging time and center coordinates from the image header file into NASA’s atmospheric modeling website (<https://atmcorr.gsfc.nasa.gov>), it is possible to acquire atmospheric transmittance and atmospheric upwelling radiance.

Atmospheric average action temperature T_a

There is a certain linear relationship between the average action temperature of the atmosphere and the air temperature 2 m above the ground. According to Qin *et.al* (2001), a linear model for calculating the average action temperature of the atmosphere (see Table 1) was proposed. The atmospheric average action temperature for each image can be calculated using the meteorological station temperature data provided by China Meteorological Data Network (<http://data.cma.cn>).

Surface specific emissivity ϵ

For surface-specific emissivity estimation, the fraction vegetation coverage FVC was derived firstly from the normalized vegetation index $NDVI$ of each image based on mixed pixel decomposition method (Sobrino *et al.* 2004) shown in Eq. (4), and finally, the surface specific emissivity of different surface types could be obtained according to FVC .

$$FVC = (NDVI - NDVI_s) / (NDVI_v - NDVI_s) \tag{4}$$

where FVC is the fraction of vegetation coverage. $NDVI_v$ and $NDVI_s$ represented the $NDVI$ threshold of the lush vegetation pixel and the bare soil pixel, respectively. The value of $NDVI_v$ is 0.7, and $NDVI_s$ is 0. When $NDVI$ is greater than or

equal to 0.7, the pixel is regarded as a complete vegetation pixel, and FVC should be 1. When $NDVI$ is less than or equal to 0, FVC should be 0.

The land surface type in remote sensing images could be roughly divided into water bodies, building, and natural surfaces (Rozenstein *et al.* 2014). Among them, the structure of water body pixels would be relatively simple, and ϵ can be fixed at 0.995. The composition of building pixels is relatively complex (a mixture of vegetation and buildings). The natural surface includes all kinds of forest, grassland, cultivated land, and bare soil, which can be regarded as a mixture of vegetation and bare soil. The equations for calculating the specific emissivity were as follows (Eqs. (5)–(7):

$$\epsilon_{water} = 0.995 \tag{5}$$

$$\epsilon_{build} = 0.9589 + 0.086F_v - 0.067F_v^2 \tag{6}$$

$$\epsilon_{surface} = 0.9625 + 0.0614F_v - 0.0461F_v^2 \tag{7}$$

where ϵ_{water} , ϵ_{build} , $\epsilon_{surface}$ represented the surface-specific emissivity of water body, building, and natural surface pixels, respectively.

Brightness temperature T

The brightness temperature was calculated by Planck’s formula shown in Eq. (8):

$$T = K_2 / \ln(K_1 / L + 1) \tag{8}$$

where T represented the brightness temperature with unit K. L represented the radiance value of the thermal infrared band. K_1 and K_2 were the constants. For Landsat 5 satellite, K_1 and K_2 would be 607.766 W/(m²•sr• μ m) and 1260.56 K, respectively. For Landsat 8 satellite, K_1 and K_2 would be 774.89 W/(m²•sr• μ m) and 1321.08 K, respectively.

UHI intensity classification

UHI effect was classified based on the LST results for analytical purposes. In order to eliminate the impact caused by temporal differences and enable comparison and analysis of LST at different times, the standard deviation method (Hanqiu Xu 2015) was adopted to determine the temperature threshold T_t shown in Eq. (9), which could represent the degree of proximity of the surface temperature of each pixel to the average surface temperature.

$$T_t = \mu + X \cdot std \tag{9}$$

where T_t was the LST threshold for UHI classification. μ was the average value of LST. std was the LST standard

Table 1 Linear models for atmospheric average action temperature

Atmospheric mode	Atmospheric average action temperature calculation model
Tropical mean atmosphere	$T_a = 17.9769 + 0.91715T_0$
Mid-latitude summer atmosphere	$T_a = 16.011 + 0.92621T_0$
Mid-latitude winter atmosphere	$T_a = 19.2704 + 0.9118T_0$
US Standard Atmosphere 1976	$T_a = 25.9396 + 0.88045T_0$

*In this table, T_0 is the air temperature 2 m above the ground, T_a indicating atmospheric average action temperature, and the unit is K

Table 2 Classification standard of LST in Jinan City

Grade division	Temperature class	UHI intensity grade
$T_i > \mu + 1.5std$	High temperature	Strong heat island effect area
$\mu + 0.5std < T_i \leq \mu + 1.5std$	Sub-high temperature	Heat island effect area
$\mu - 0.5std \leq T_i \leq \mu + 0.5std$	Medium temperature	No obvious effect area
$\mu - 1.5std \leq T_i < \mu - 0.5std$	Sub-low temperature	Cold island effect area
$T_i < \mu - 1.5std$	Low temperature	Strong cold island effect area

deviation. X represented the multiple of the LST standard deviation.

The values of X were 0.5 and 1.5 according to the grades defined in this study. The estimated LST in Jinan City was further classified into five UHI intensity grades: strong heat island effect area, heat island effect area, no obvious effect area, cold island effect area, and strong cold island effect area. Table 2 shows the specific grading standards.

Results

LST results and validation

The estimated LST for each period of images and the corresponding meteorological station data are shown in Table 3. By comparing them in Fig. 3, it was found that the RMSE between the inversion results from the remote sensing images and the measurements from the meteorological station was 3.6 °C, indicating the higher inversion accuracy. Therefore, it is feasible to conduct a spatiotemporal analysis of the UHI effect in Jinan City based on the LST inversion results from the remote sensing images. To further validate the accuracy of land surface temperature inversion, this study used the MOD11A1 dataset from NASA’s website

Table 3 Comparison of inversed LST results and meteorological station data in Jinan City

Image date	Estimated LST(°C)	Meteorological station data (°C)
2009–04-08	18.4	22.80
2009–08-30	17.6	22.00
2009–10-17	16.3	17.60
2009–11-02	-1.2	3.50
2014–03-21	14.6	16.30
2014–07-11	30.2	34.30
2014–10-15	16.9	19.70
2014–12-18	-0.2	2.90
2019–05-22	29.9	34.80
2019–06-07	28.7	33.30
2019–10-29	12.9	14.50
2019–11-14	8	10.30

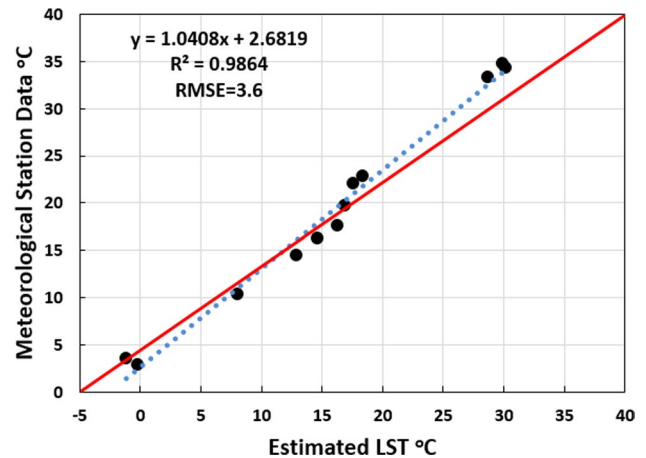


Fig. 3 The comparison of estimated LST with measured temperature from the meteorological station

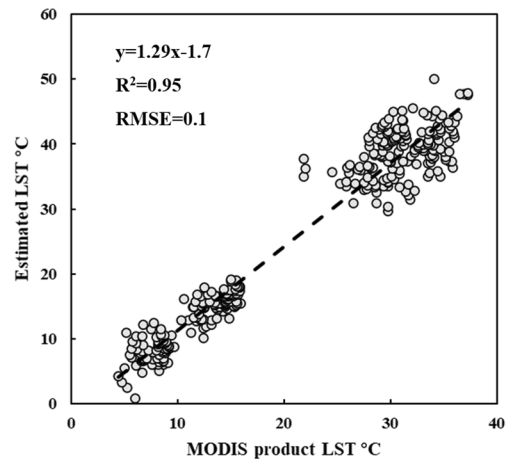


Fig. 4 The comparison of estimated LST with MODIS product LST

(<https://ladsweb.modaps.eosdis.nasa.gov/>) as validation data. After resampling, comparative analysis showed a correlation coefficient exceeding 0.9 and a root mean square error of 0.1 °C between the two datasets shown in Fig. 4.

Through the UHI distribution in Jinan City shown in Fig. 5, the temperature difference between urban and suburban areas in Jinan City was noticeable in spring and summer. Especially in summer, not only was the area of heat island

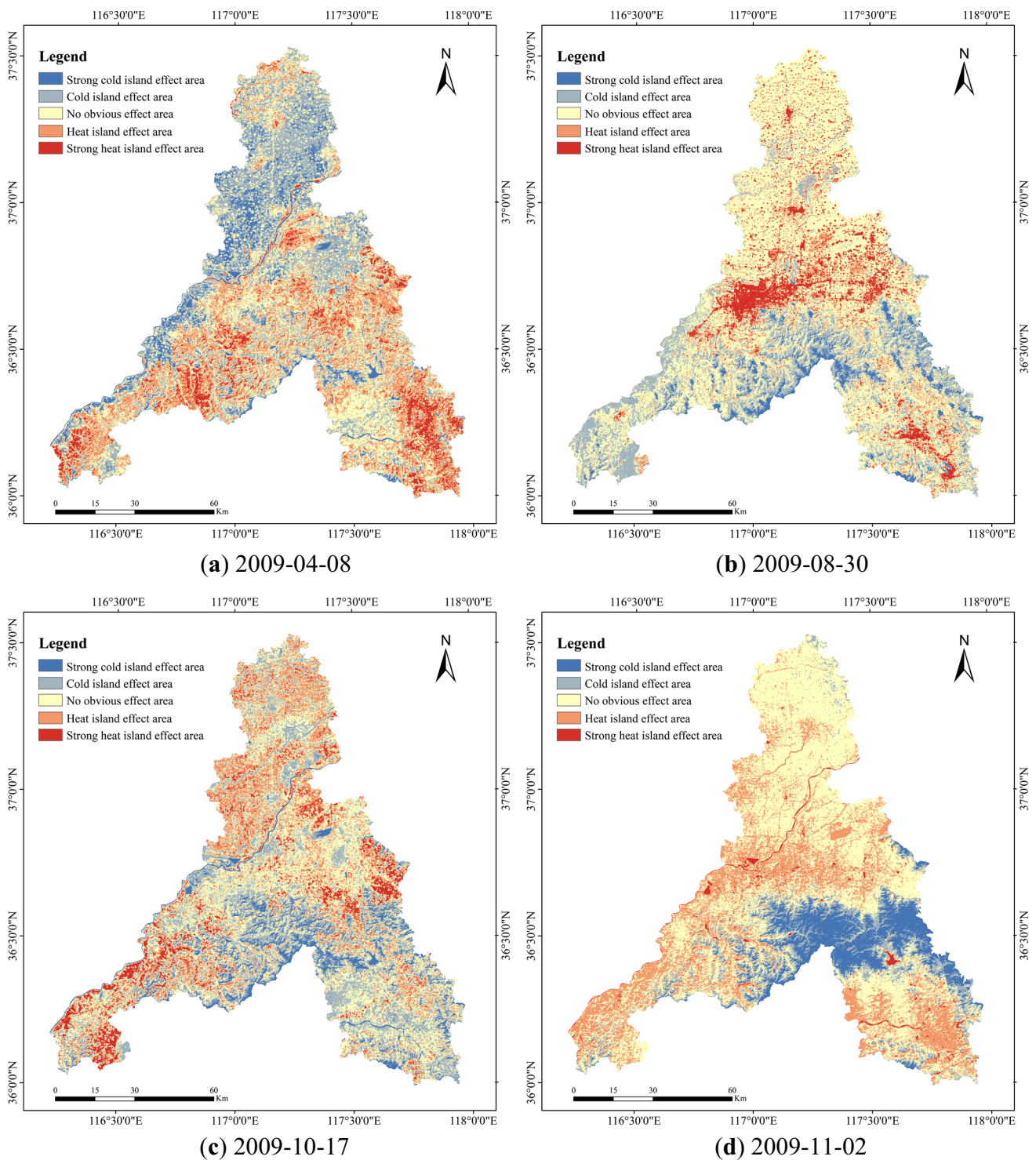


Fig. 5 UHI distribution in Jinan City in 2009

wider, but also the urban region had a higher concentration of significant heat islands. On the contrary, Jinan’s heat island effect was less noticeable in fall and winter. The urban heat island boundary in Jinan City was evident in 2009, with broad strong heat island areas in the central urban area. Heat

island areas in Gangcheng and Laiwu districts were interconnected, while Changqing and Zhangqiu districts were linked to the main urban area via various transportation routes. The central regions of neighboring counties and districts also featured isolated patches of high-temperature zones.

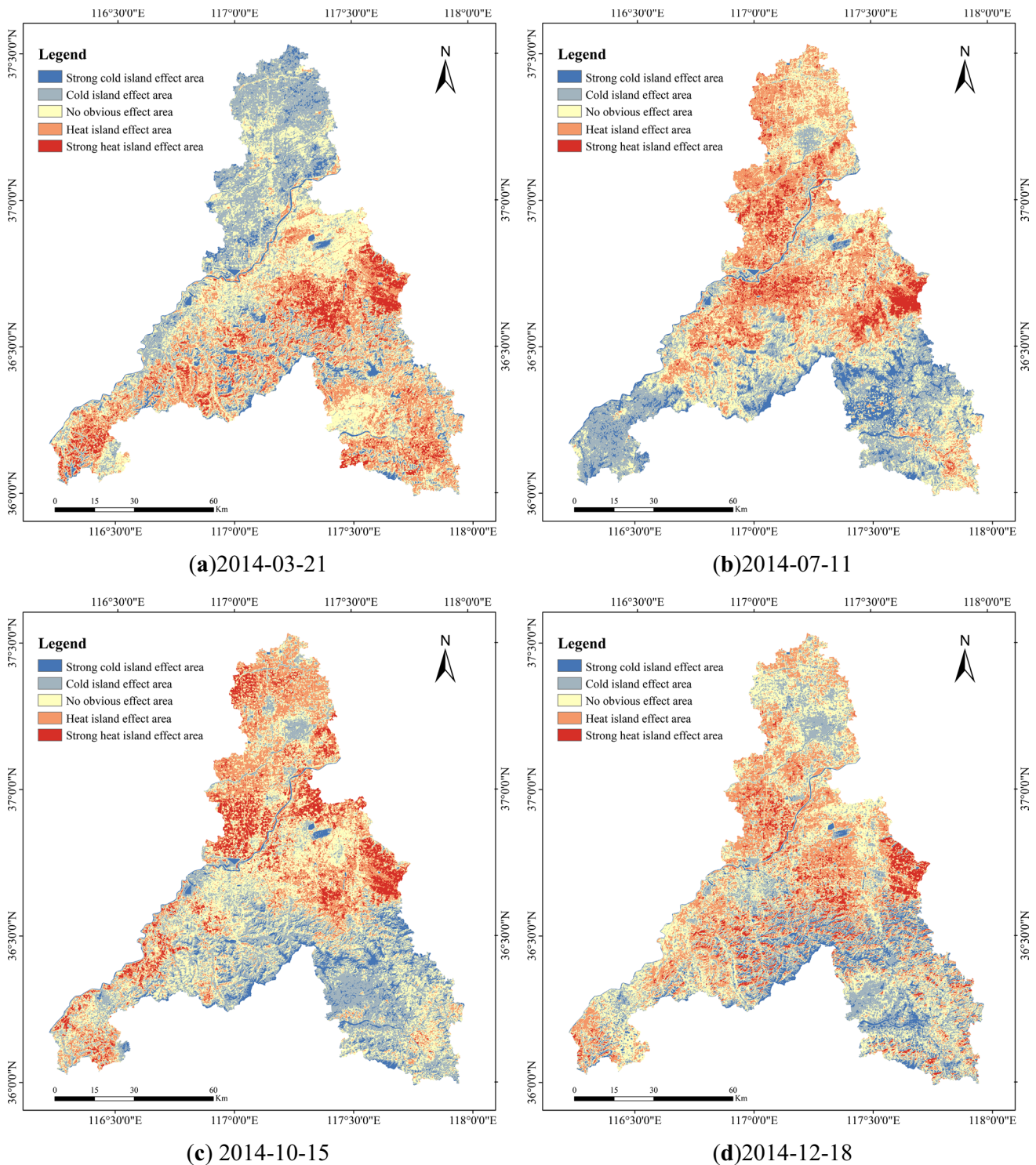


Fig. 6 UHI distribution in Jinan City in 2014

As illustrated in Fig. 6, the urban heat island effect was the strongest in the summer of 2014. The urban heat island only appeared in some areas of Jinan in spring and autumn. There was a significant disparity between the south and north areas. No obvious heat island

phenomenon was observed in winter. Even in the city heart, there were some cold islands. The general extent of the UHI effect extended in 2014, with a noteworthy increase in severity, particularly in Changqing and Zhangqiu districts.

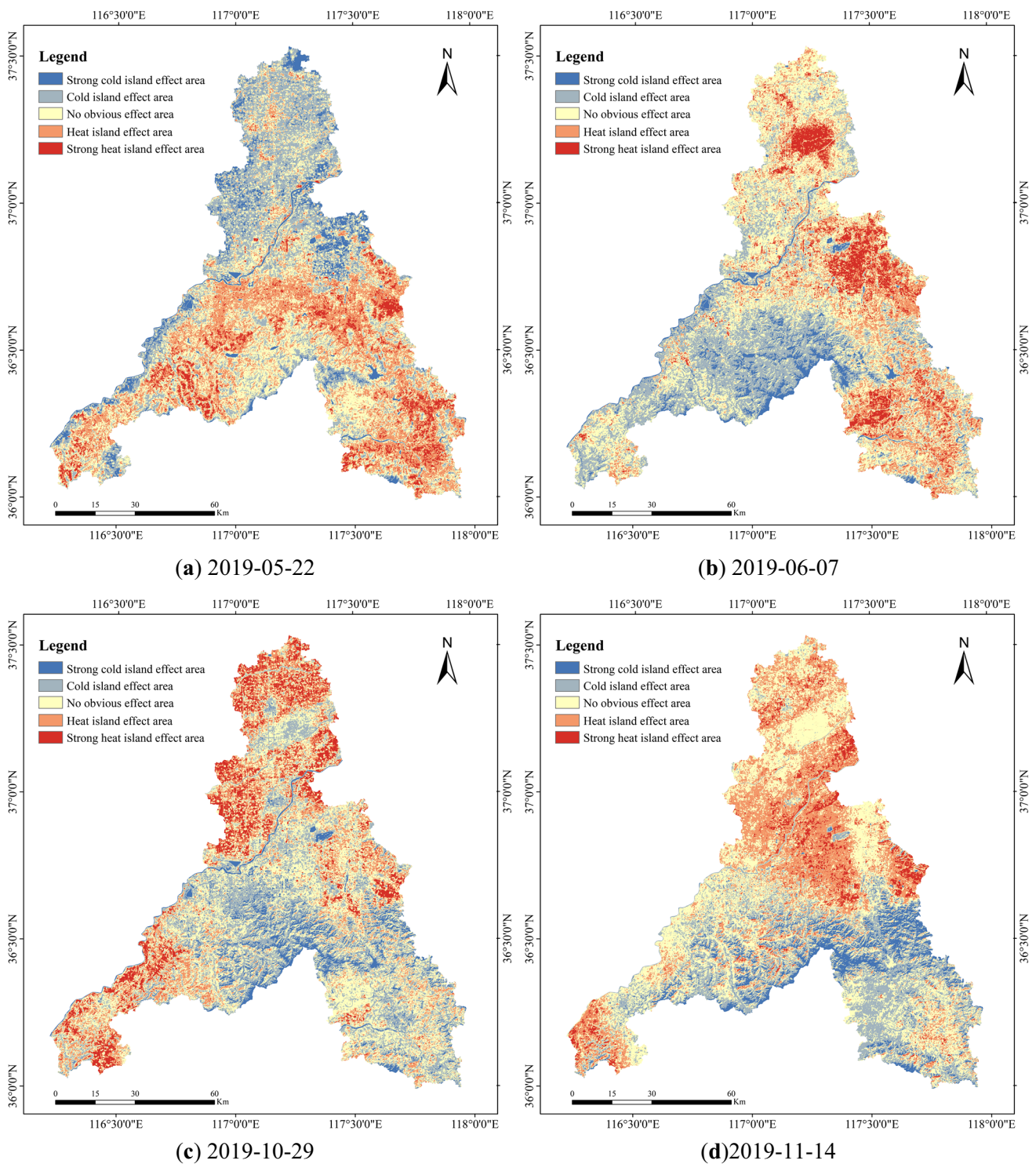


Fig. 7 UHI distribution in Jinan City in 2019

Figure 7 shows a very typical heat island phenomenon that occurred in spring, while there was no heat island effect in summer. The air and ground temperatures were also lower, which may be affected by the weather at the time of image generation. In 2019, the UHI area in Jinan City expanded

further, with the heat island effect in Changqing and Zhangqiu districts being practically continuous with the city core. The high-temperature zones in Shanghe County, Jiyang District, Pingyin County, Laiwu District, and Gangcheng District also experienced significant growth.

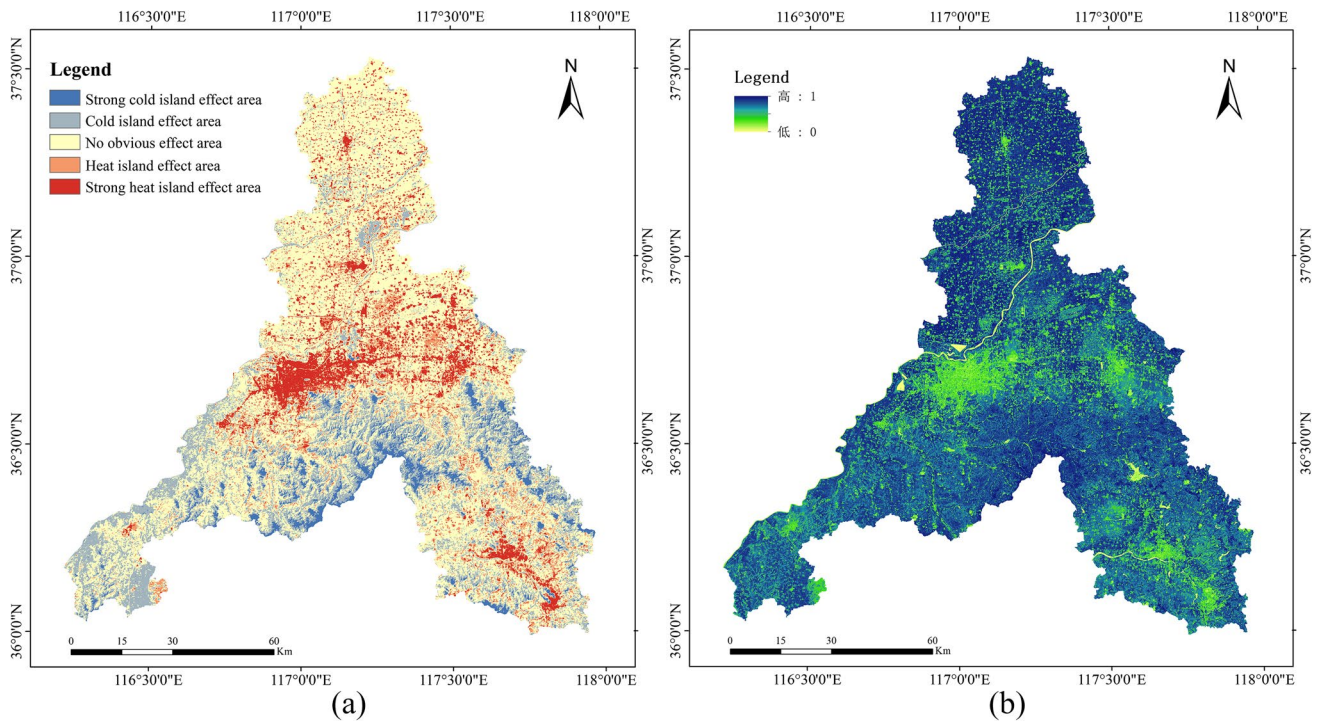


Fig. 8 Comparison of UHI intensity (a) and fraction vegetation coverage (b) in Jinan City in 2009

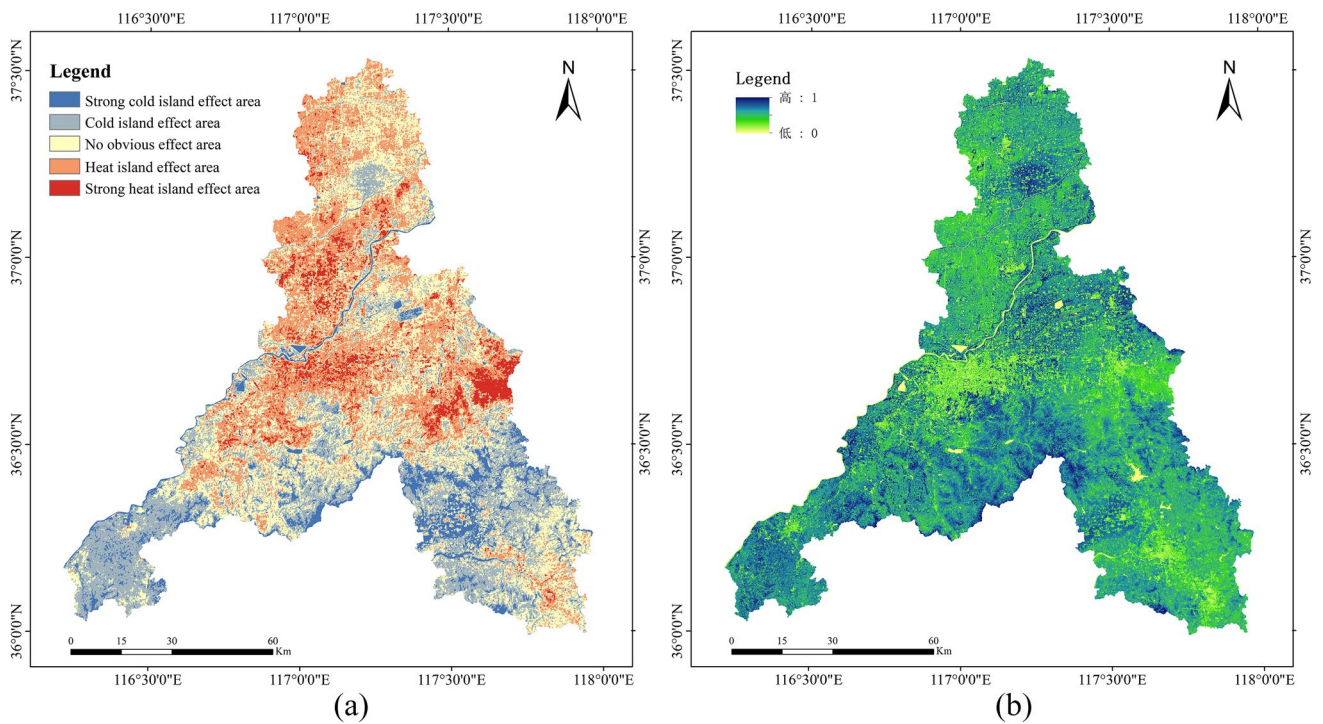


Fig. 9 Comparison of UHI intensity (a) and fraction vegetation coverage (b) in Jinan City in 2014

Over the 10-year period from 2009 to 2019, the UHI effect in Jinan City exhibited a clear intensification, showing a strong correlation with the city’s overall development trends and planning. In addition, the UHI effect often occurs in spring and summer in Jinan City. The temperature in the major part of Jinan City, Tianqiao District, Huaiyin District, Shizhong District, and Lixia District was much higher than in other regions at this time, while the southern mountainous area remained a cold island state throughout the year.

In order to explore the factors influencing the UHI effect in Jinan City, this study utilized land cover types such as vegetation, water bodies, and urban buildings to analyze the evolution of the UHI effect pattern. The findings aim to provide technical guidance for mitigating the UHI effect.

Relationship between the UHI effect and the fraction vegetation coverage

Landsat images from the same period as the aforementioned UHI intensity distribution map were selected. The fraction vegetation coverage in the study area was extracted respectively shown in Eq. (4), and compared with the distribution of UHI intensity.

Upon comparing Figs. 8, 9, and 10, it was observed that the areas with low fraction vegetation coverage were more consistent with the areas with obvious UHI effect, demonstrating a negative relationship between fractional vegetation coverage and urban surface temperature. In addition, the inversed LST results and fraction vegetation coverage data on May 22, 2019, were utilized to conduct quantitative correlation analysis on the relationship between LST and fraction vegetation coverage, with 340-pixel samples being selected from all types of pixels other than water bodies. The correlation analysis results shown in Fig. 11 revealed that the Pearson correlation coefficient between the two was -0.732 (significant correlation at the p -value 0.01 level), showing that the effect of vegetation lushness on LST was more obvious, and the two demonstrated a negative association, implying that locations with more vegetation coverage had lower surface temperature.

Relationship between UHI effect and water body

In terms of the relationship between the UHI effect and the water body, it is worth noting that regions with low surface fraction vegetation coverage are usually accompanied by higher surface temperatures. However, water

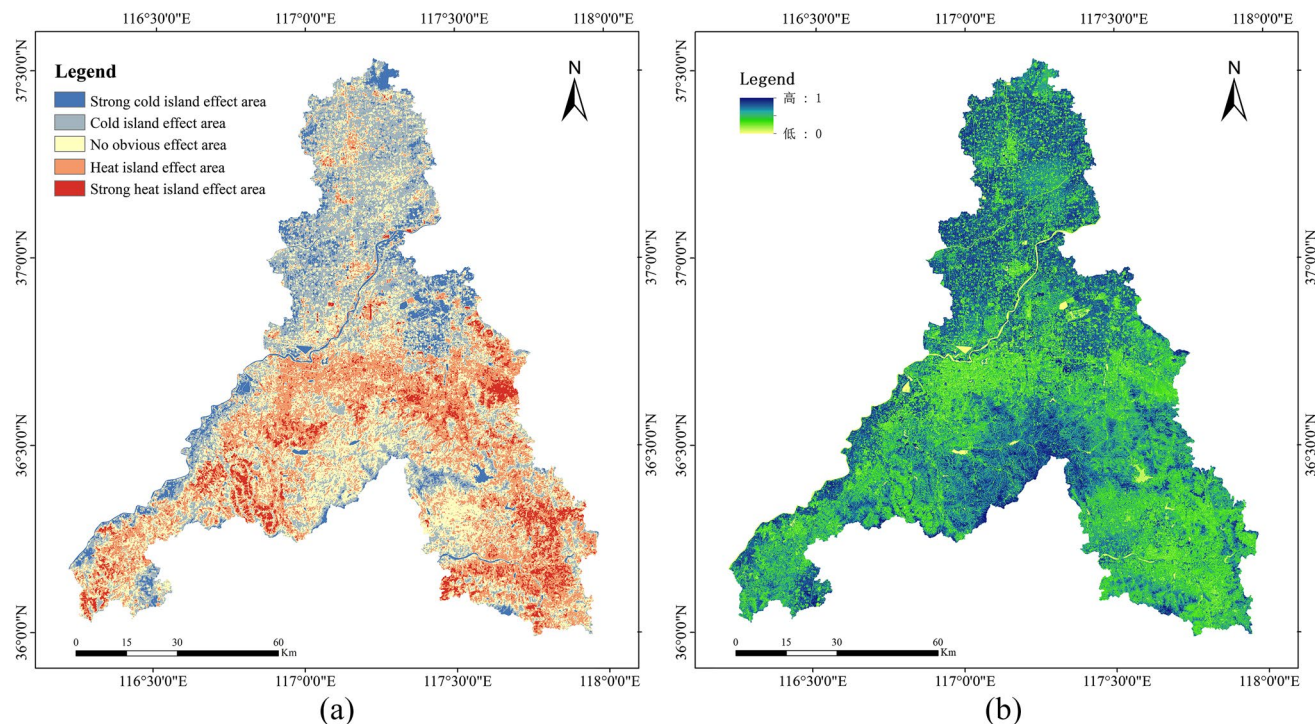


Fig. 10 Comparison of UHI intensity (a) and fraction vegetation coverage (b) in Jinan City in 2019

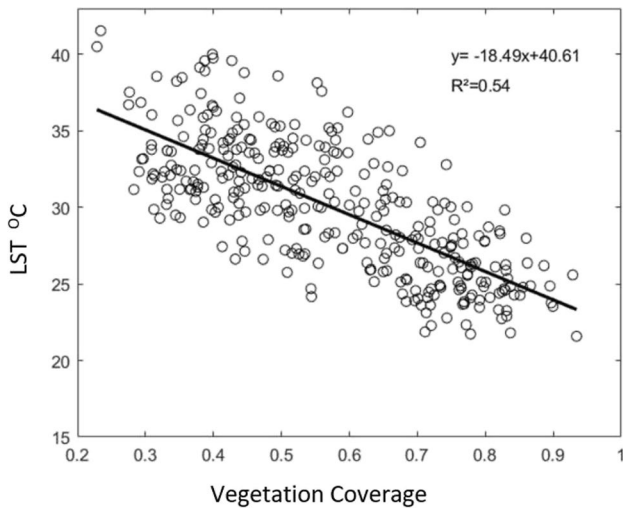


Fig. 11 Linear regression relationship between LST and fraction vegetation coverage

locations frequently have a low fraction of vegetation coverage, with no vegetation pixels present, and the water environment in urban areas frequently functions as a temperature regulator and aids in alleviating high temperatures. Therefore, the UHI effect in the water area was studied utilizing the distribution of the water body in Jinan City shown in Fig. 12.

By utilizing the vector file of the water body distribution in Jinan City, the corresponding regional UHI classification data was obtained. The distribution of heat island grades in the water body area was further counted and presented in Fig. 13.

Table 4 indicates that water bodies in Jinan City exhibited strong cold island effects. The combined area of strong cold island effects and cold island effects within water bodies amounts to 89.7%. Referring to Fig. 13, the Yellow River, Tuhai River, Xiaoqing River, Mouwen River, and other rivers in Jinan City exhibit a winding

Fig. 12 Water body distribution in Jinan City

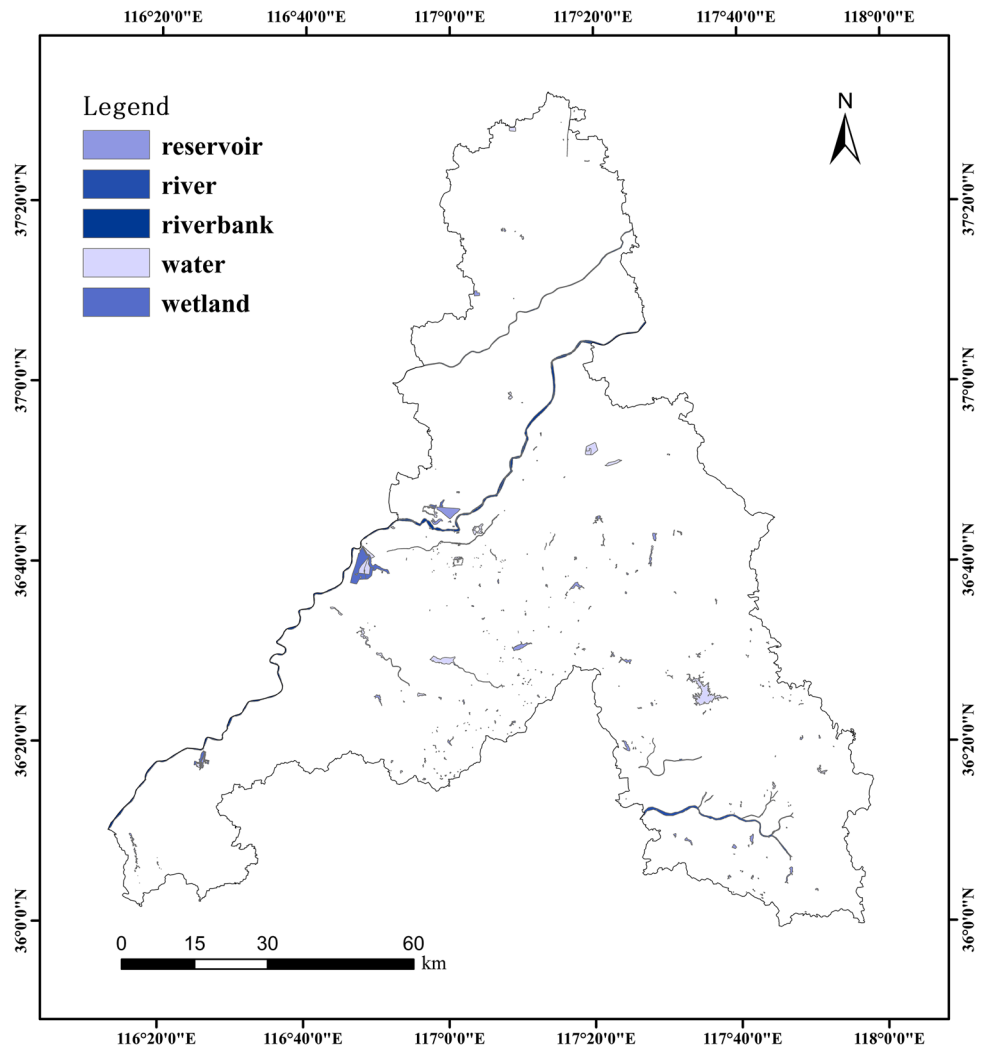
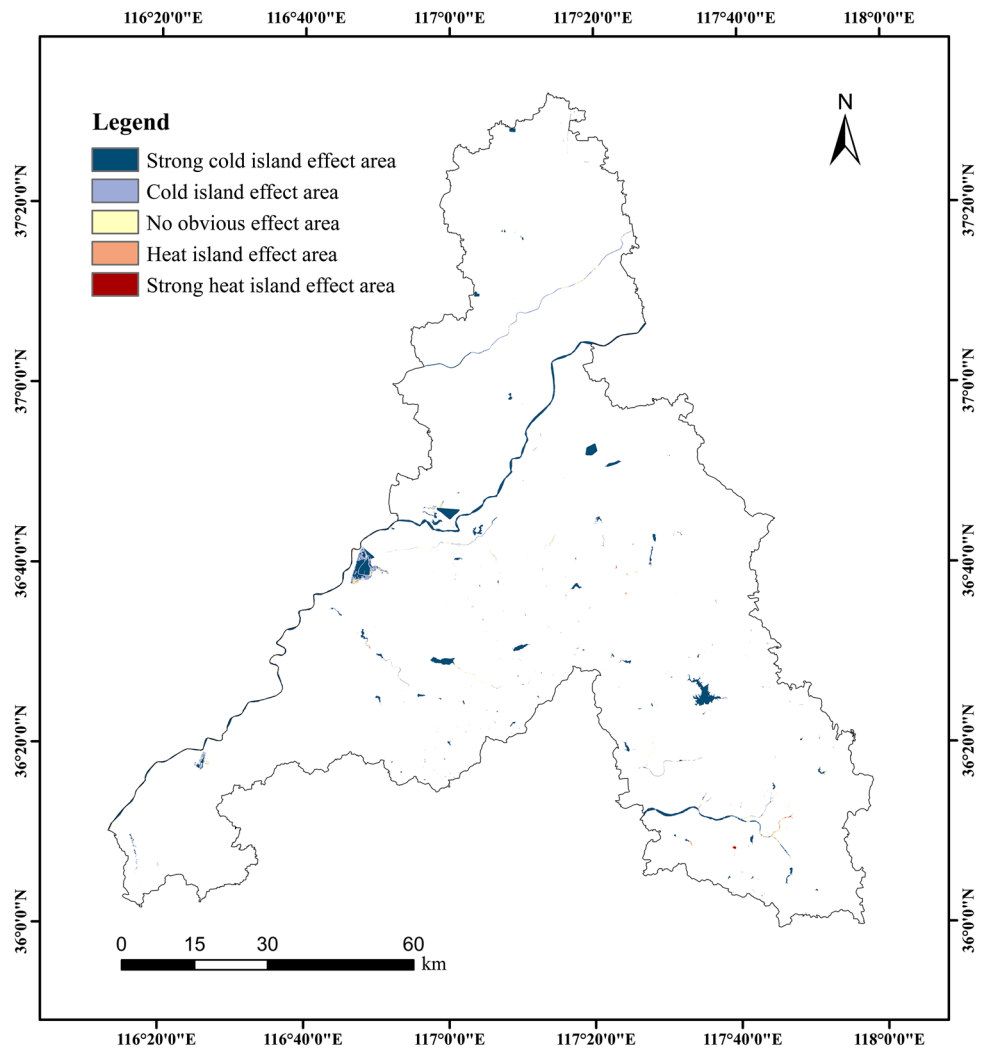


Fig. 13 Distribution of UHI intensity in the water area of Jinan City in 2019



distribution of cold islands. Irregularly shaped reservoirs and lakes also align well with the corresponding cold island areas. In addition, wetland areas also demonstrated a cold island phenomenon, with larger individual areas, contributing significantly to the cooling effect in conjunction with other water bodies.

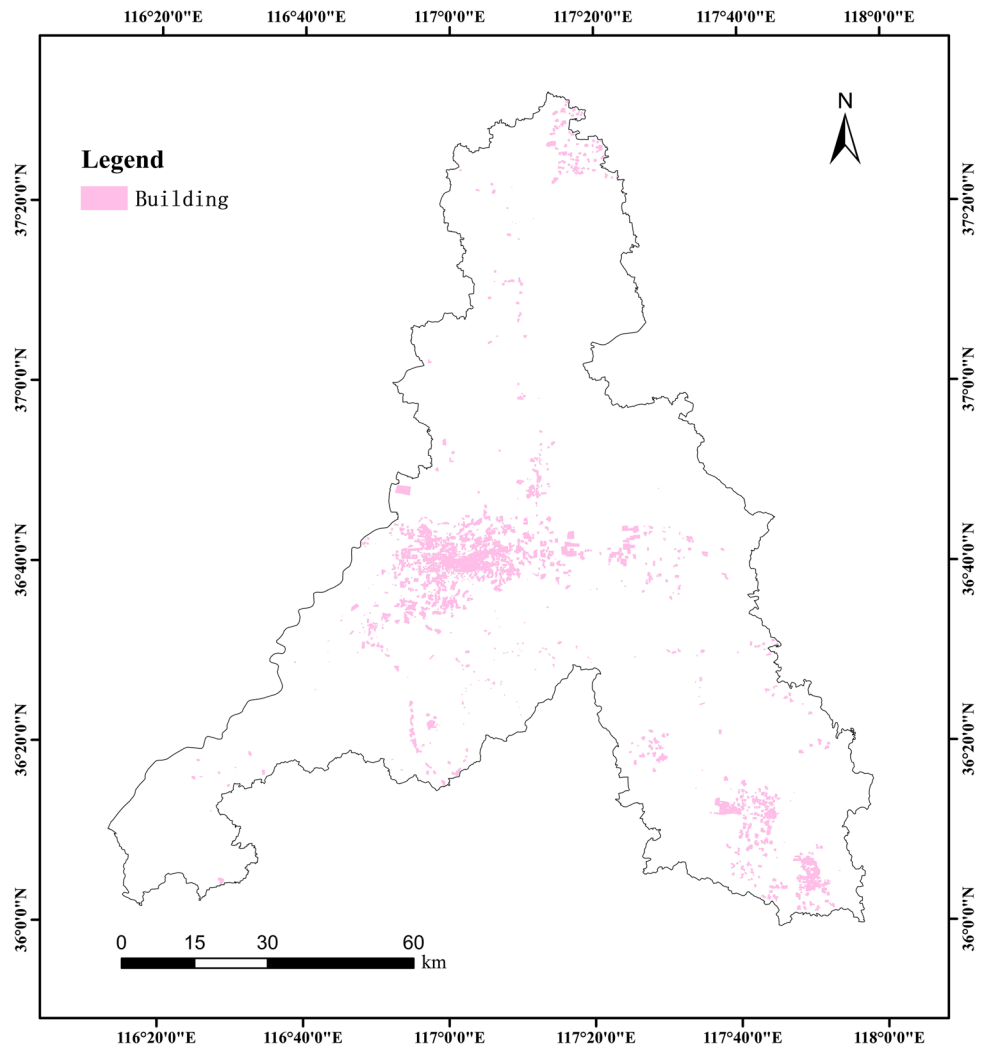
Table 4 The distribution of UHI intensity in water area

UHI intensity grade	Number of pixels	Percentage
Strong heat island effect area	438	0.2%
Heat island effect area	3701	2.0%
No obvious effect area	14,822	8.1%
Cold island effect area	40,252	22.0%
Strong cold island effect area	124,100	67.7%

Relationship between UHI effect and urban buildings

Using the data of commercial, medical, industrial, and residential buildings in Jinan City, the association between building dispersion shown in Fig. 14 and the UHI effect was analyzed. By extracting the UHI intensity raster data of the corresponding area from the vector file of building distribution in Jinan City, the UHI effect area of each grade in the building area can be obtained. The distribution of UHI grades in the building area in Jinan City was further calculated, as shown in Fig. 15 and Table 5. Figure 15 illustrates that buildings were strongly associated with a considerable number of heat island areas. Table 5 showed that heat island and strong heat island effect areas constituted 62.2% of the

Fig. 14 Building distribution in Jinan



total area, while cold island and strong cold island effect areas accounted for less than 3%. The presence of high-temperature areas within the building distribution range indicated that human factors significantly contributed to the formation of urban heat islands. The rapid urbanization process has resulted in a rise in the UHI effect.

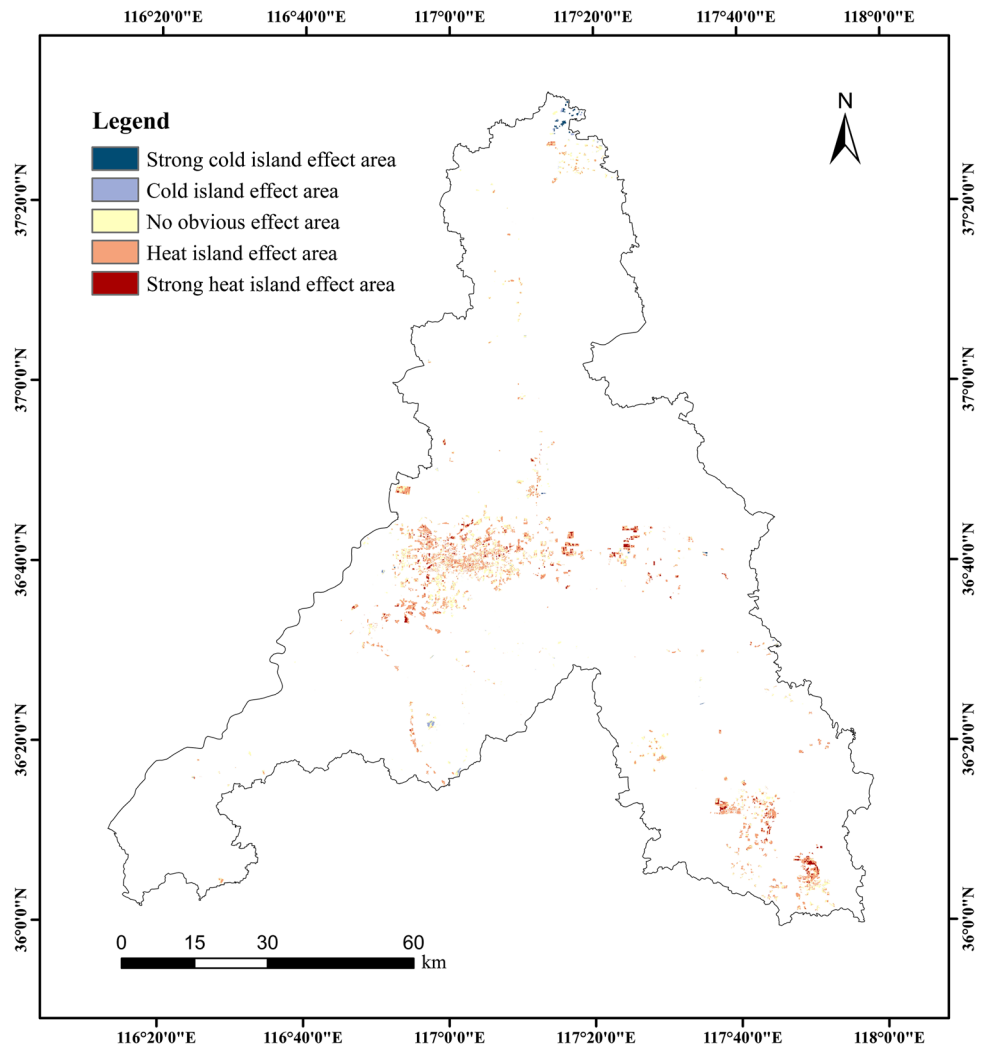
Discussion

Spatiotemporal analysis of UHI effect

It can be seen from Fig. 16 that Jinan City's urban and suburban areas exhibited notable trends in temperature anomalies from 2009 to 2019. In the urban area, temperature anomalies decreased from -0.246 in 2009 to -1.176 in 2013, sharply

rose to 1.244 in 2014, and continued to increase to 1.144 by 2019, indicating a consistent warming trend. Concurrently, the urban area's 2a moving average increased from 20.115 in 2010 to 21.22 in 2019, reflecting an overall temperature rise. In contrast, suburban temperature anomalies also showed negative values from 2009 to 2013, declining from -0.341 to -1.231 , followed by a shift to positive anomalies starting in 2014, peaking at 1.469 by 2019, indicating a pronounced upward trend. The suburban 2a moving average increased from 20.065 in 2010 to 21.515 in 2019, slightly higher than that of the urban area, possibly reflecting a faster temperature increase due to urban expansion and rural development. In conclusion, both urban and suburban areas demonstrated a warming trend, with suburbs showing slightly greater variability, likely influenced by the processes of urbanization and their impacts on regional climate.

Fig. 15 The distribution of heat island intensity in the building area of Jinan in 2019



Urban heat island intensity refers to the temperature difference between urban and rural areas caused by the urban heat island effect, represented by UHI. UHI is calculated in Eq. (10).

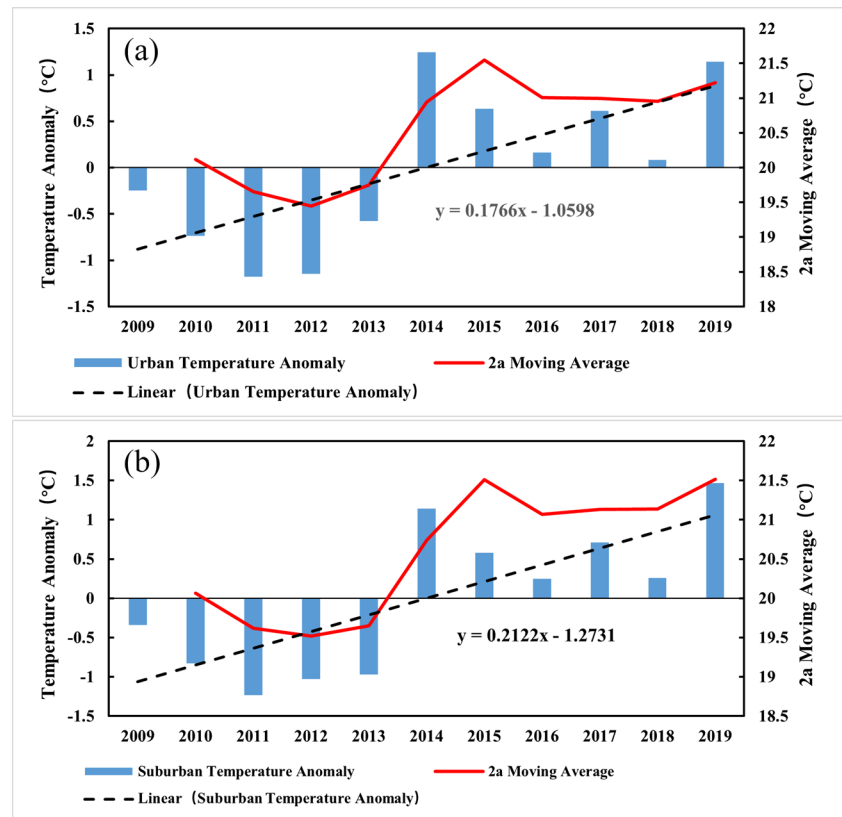
$$UHI = T_{urban} - T_{suburban} \tag{10}$$

Table 5 The distribution of UHI intensity in the building area

UHI intensity grade	Number of pixels	Percentage
Strong heat island effect area	20,319	7.0%
Heat island effect area	161,039	55.2%
No obvious effect area	102,535	35.1%
Cold island effect area	4944	1.7%
Strong cold island effect area	2927	1%

UHI effect data in Jinan shown in Fig. 17 demonstrated significant changes from 2009 to 2019. Through the 2-year moving average (2a moving average), it can be seen that from 2009 to 2011, the UHI values were relatively stable with little change. In 2012, the UHI value dropped sharply and turned negative, indicating that urban temperatures were lower than suburban temperatures. In 2013, the UHI value rebounded and reached the highest value of 0.35. From 2014 to 2015, the UHI value fell again but remained positive. From 2016 to 2019, the UHI value continued to decline, reaching a low of -0.37 in 2019, indicating that urban temperatures were significantly lower than suburban temperatures. The 2-year moving average further smoothed these changes, showing an overall downward trend, especially with the prolonged period of negative values after 2016.

Fig. 16 Annual mean temperature anomaly in urban (a) and suburban (b) areas of Jinan City from 2009 to 2019



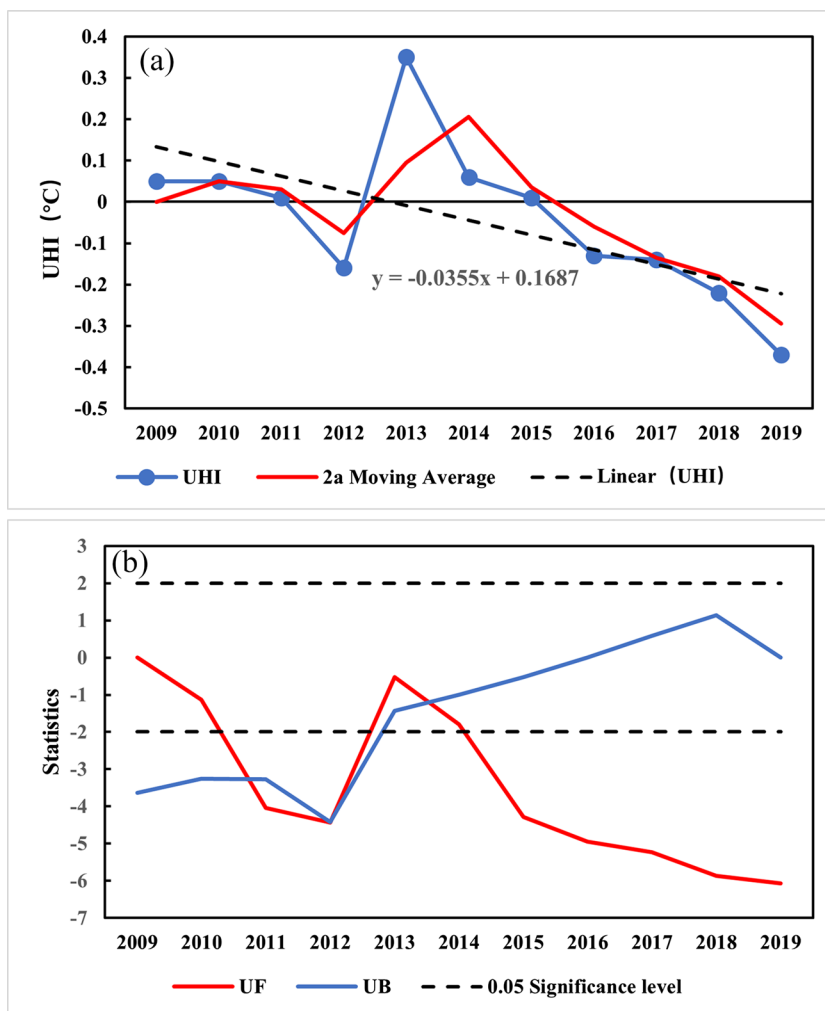
Through the Mann–Kendall (M–K) trend test analysis, the comparison of UF and UB values shows that from 2009 to 2011, both UF and UB values were negative, indicating a downward trend in UHI values during this period. In 2012, both UF and UB values dropped sharply, further confirming the significant decline in UHI values. In 2013, the UF value turned positive, but the UB value remained negative, indicating an upward trend in UHI values, although the trend was not stable. In 2014, the UF value turned negative again, indicating that the upward trend in UHI values did not continue. From 2015 to 2019, both UF and UB values were negative and declined year by year, confirming the long-term downward trend in UHI values. 2010, 2011, and 2012 are the intersection years of UF and UB values, indicating that these years are important turning points in the trend change.

Combining the UHI data and the M–K analysis results, it can be concluded that the UHI value in Jinan was relatively stable before 2012, with a significant decline in 2012. Although there was a short rebound in 2013, the overall trend remained downward. After 2016, the UHI

value remained negative for a long time, indicating that urban temperatures were generally lower than suburban temperatures. The M–K analysis results (UF and UB values) are consistent with the actual UHI data trends, both indicating that Jinan’s urban heat island effect showed an overall downward trend from 2009 to 2019, especially with a more pronounced downward trend after 2016.

As can be seen from Fig. 18, from 2009 to 2019, the average seasonal temperatures in Jinan showed an overall increase: spring temperatures rose from 5.3 to 7.3 °C, summer temperatures increased from 23.6 to 25.2 °C, autumn temperatures fluctuated between 31.7 and 33.6 °C, and winter temperatures rose from 20.7 to 22.0 °C. The UHI effect in spring increased from 0.01 to 0.25, while in summer, autumn, and winter, it decreased from 0.2 to –0.4, from –0.1 to –0.8, and from 0.6 to –0.6, respectively. This indicates that except for spring, the temperature in suburban areas increased faster than in urban areas, possibly due to urban expansion and rural area development.

Fig. 17 Annual mean UHI change and M–K mutation test in Jinan City



Influencing factors of UHI effect in Jinan City

The Geodetector (Wang and Xu 2017) is a statistical tool used to reveal spatial distribution patterns and their driving factors. It assesses their influence and significance by analyzing the explanatory power of different factors on the target variable. This study uses factor detection to analyze the impact of vegetation coverage, land cover classification, DEM, and precipitation on the heat island effect.

$$q = 1 - \frac{\sum_{h=1}^L N_h \sigma_h^2}{N \sigma^2} \tag{11}$$

In Eq. (11), the *q* value ranges from [0,1], indicating the extent of influence of the impact factors on the target variable. The larger the *q* value, the stronger the influence.

To investigate the influencing factors of UHI intensity levels in Jinan, Geodetector was introduced, and the intensity level of the urban heat island effect was used as the dependent variable *Y*. FVC, land cover, DEM, and slope were used as independent variables *X*₁ to *X*₄, before running the Geodetector, FVC, DEM, and slope were discretized into five categories. The results of factor detection are shown in Fig. 19 and Table 6, the influence of FVC on the intensity level of the UHI effect is consistently the greatest among all factors across the three time points, and the average *q*-value is 0.25. The influence of the three factors land cover, DEM, and slope all reached their maximum values in 2014. The influence of precipitation has been steadily increasing year by year.

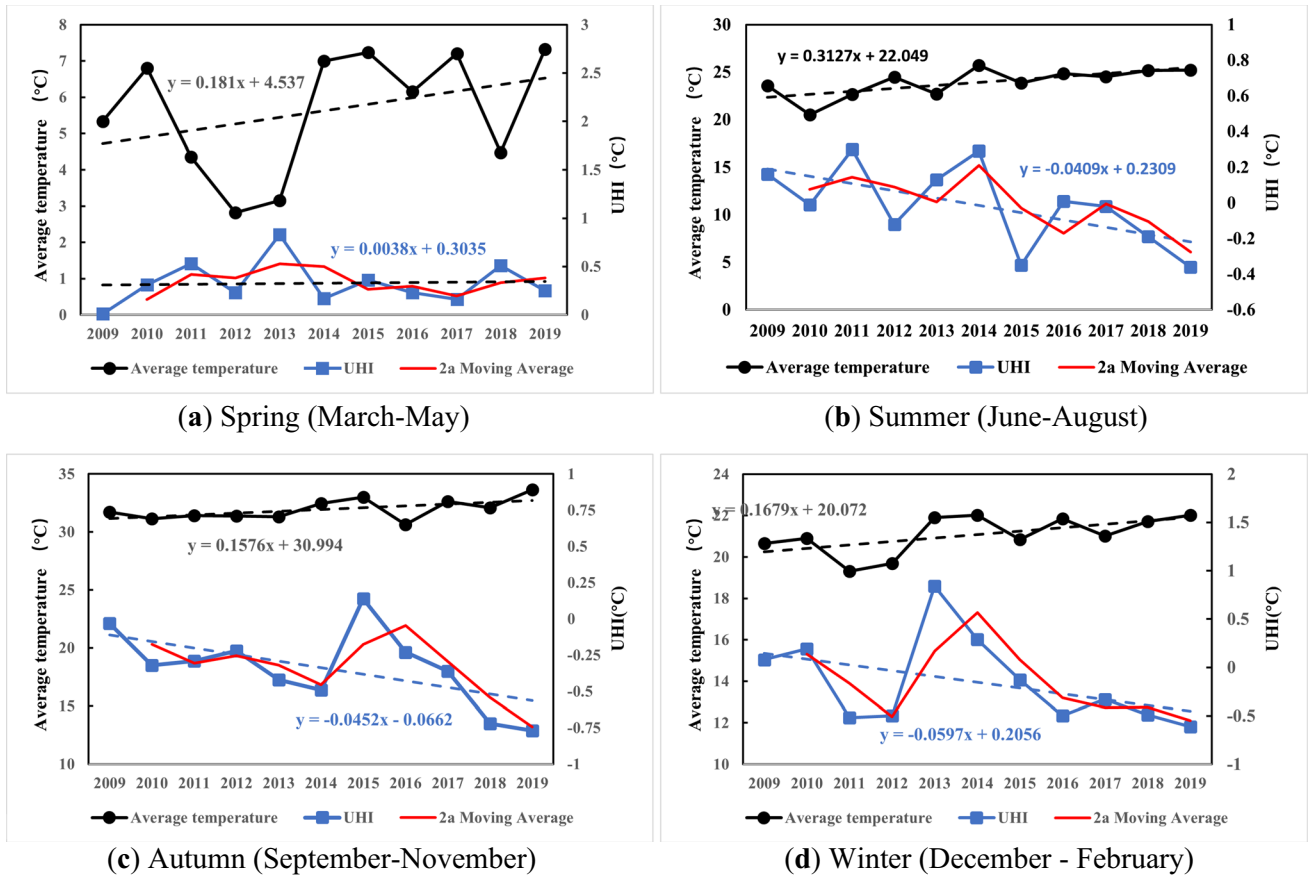


Fig. 18 Average temperature and UHI changes in spring (a), summer (b), autumn (c), and winter (d) in Jinan

Fig. 19 Influencing factors of different variables

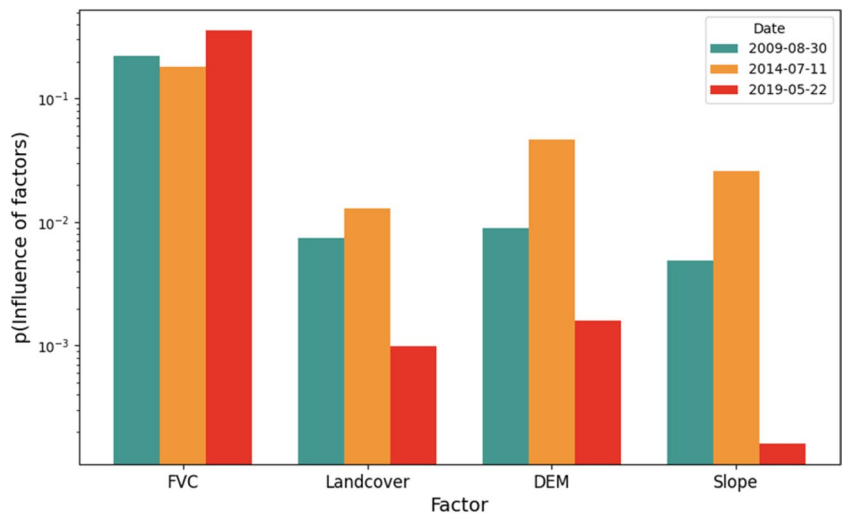


Table 6 Influencing factors of different variables

Influence of factors	Time		
	2009/8/30	2014/7/11	2019/5/22
X1(FVC)	0.2222	0.187	0.3570
X2(Landcover)	0.0074	0.0130	0.0010
X3(DEM)	0.0090	0.0466	0.0016
X4(Slope)	0.0049	0.0261	0.0002

Note: All data in the table passed the p -test ($p < 0.01$)

Conclusions

The study investigated the spatiotemporal characteristics of the UHI effect in Jinan City using Landsat TM and OLI/TIRS remote sensing data based on the mono-window algorithm. The surface temperature data of Jinan City were collected for four seasons in 2009, 2014, and 2019 and were coupled with distribution data of urban buildings, vegetation coverage, and water bodies to examine the temporal and spatial fluctuation characteristics of the UHI effect in Jinan City. According to the findings, the UHI effect in Jinan was relatively significant in the spring and summer, especially in the summer, but weaker in the autumn and winter. The primary heat island coverage area was in the city center, including Lixia District and surrounding areas. The research further indicated that the UHI effect was strongly influenced by the urban surface type. UHI was inhibited by vegetation and water bodies, whereas regions with more buildings tended to have a larger UHI effect. In the Geodetector analysis results, FVC exhibits the strongest influence on the intensity level of the urban heat island effect among all factors, with an average q -value of 0.25. The Pearson correlation coefficient between FVC and LST is -0.732 . The combined area of strong cool island effect zones and cool island effect zones within water bodies is 89.7%. The combined proportion of heat island and strong heat island effect zones in building areas is 62.2%. FVC and land cover classification significantly affect heat island intensity, with a Pearson correlation coefficient of -0.732 between FVC and LST. The areas with strong cool island effects and cool island effects within the water body together account for 89.7%, while the combined proportion of heat island and strong heat island effect zones in building areas is 62.2%.

Although the mono-window algorithm used in this study had obtained better surface temperature inversion results for TM and OLI/TIRS images, the research still has some limitations. The data selection was affected by image cloud and fog, and the surface temperature measured by the meteorological station may differ from the sampling of the Landsat satellite during the transit time. Future research can improve the results by on-site measurement during the satellite transit time.

Acknowledgements Thanks to Shandong Normal University for its cultivation and support.

Author contribution Guiquan Mo and Yurong Cui wrote the text of the main manuscript and compiled the charts. Libo Yan and Zongyao Wang conducted research guidance and improved the analysis and content of the manuscript. Guiquan Mo contributed to the data analysis and the writing of the manuscript. Zhiyong Li, Sixuan Chen, and Shuwei Zheng conducted data processing. Huixuan Li contributed to the writing and revised the manuscript.

Funding This research was funded by the Technology Department of Shandong Normal University, grant number 304–0111107.

Data availability Landsat satellites data from USGS Earth Explorer (<https://earthexplorer.usgs.gov>). Vector data from Resource and Environmental Science and Data Center of the Chinese Academy of Sciences (<http://www.resdc.cn>). Land cover classification data from the Zenodo Open Science Data Sharing Platform (<https://zenodo.org/>). DEM data from Geospatial Data Cloud (<https://www.gscloud.cn/>). Precipitation data from the National Tibetan Plateau Data Center (<https://data.tpdc.ac.cn/>). Vector files of Jinan's road network, railways, buildings, water bodies, etc. from OpenStreetMap (<https://openmaptiles.org/>).

Declarations

Ethics approval and consent to participate All of the authors have carefully read and approved the paper.

Consent for publication All of the authors have agreed to publish the manuscript.

Competing interests The authors declare no competing interests.

References

- Ding N, Zhang Y, Wang Y, Chen L, Qin K, Yang X (2023) Effect of landscape pattern of urban surface evapotranspiration on land surface temperature. *Urban Climate* 49. <https://doi.org/10.1016/j.uclim.2023.101540>
- Kim SW, Brown RD (2021) Urban heat island (UHI) intensity and magnitude estimations: a systematic literature review. *Sci Total Environ* 779:146389. <https://doi.org/10.1016/j.scitotenv.2021.146389>
- Kustas W, Anderson M (2009) Advances in thermal infrared remote sensing for land surface modeling. *Agric for Meteorol* 149:2071–2081. <https://doi.org/10.1016/j.agrformet.2009.05.016>
- Liang L, Tan B, Li S, Kang Z, Liu X, Wang L (2022) Identifying the driving factors of urban land surface temperature. *Photogramm Eng Remote Sensing* 88:233–242. <https://doi.org/10.14358/PERS.21-00043R3>
- Peng S (2020) 1-km monthly precipitation dataset for China (1901–2022). *Nat Tibetan Plateau/third Pole Environ Data Center*. <https://doi.org/10.5281/zenodo.3185722>
- Qiao Z, Zhang D, Xu X, Liu L (2019) Robustness of satellite-derived land surface parameters to urban land surface temperature. *Int J Remote Sens* 40:1858–1874. <https://doi.org/10.1080/01431161.2018.1484962>
- Qin Z, Karnieli A, Berliner P (2001) A mono-window algorithm for retrieving land surface temperature from Landsat TM data and its application to the Israel-Egypt border region. *Int J Remote Sens* 22:3719–3746. <https://doi.org/10.1080/01431160010006971>
- Rozenstein O, Qin Z, Derimian Y, Karnieli A (2014) Derivation of land surface temperature for Landsat-8 TIRS using a split

- window algorithm. *Sensors* 14:5768–5780. <https://doi.org/10.3390/s140405768>
- Ru C, Duan S-B, Jiang X-G, Li ZL, Huang C, Liu M (2023) An extended SW-TES algorithm for land surface temperature and emissivity retrieval from ECOSTRESS thermal infrared data over urban areas. *Remote Sensing of Environ* 290. <https://doi.org/10.1016/j.rse.2023.113544>
- Sobrino JA, Jiménez-Muñoz JC, Paolini L (2004) Land surface temperature retrieval from LANDSAT TM 5. *Remote Sens Environ* 90:434–440. <https://doi.org/10.1016/j.rse.2004.02.003>
- Wan Z (2014) New refinements and validation of the collection-6 MODIS land-surface temperature/emissivity product. *Remote Sens Environ* 140:36–45. <https://doi.org/10.1016/j.rse.2013.08.027>
- Wang J, Xu C (2017) Geodetector: principle and prospective. *Acta Geographica Sinica* 72(1):116–134. <https://doi.org/10.11821/dlxb201701010>
- Wang J, Wang W, Zhang S, Wang Y, Sun Z, Wu B (2023) Spatial and temporal changes and development predictions of urban green spaces in Jinan City, Shandong. *China Ecol Indic* 152:110373. <https://doi.org/10.1016/j.ecolind.2023.110373>
- Xu H (2015) Retrieval of the reflectance and land surface temperature of the newly-launched Landsat 8 satellite. *Chin J Geophys (in Chinese)* 58:741–747. <https://doi.org/10.6038/cjg20150304>
- Yamamoto Y, Ishikawa H (2018) Thermal land surface emissivity for retrieving land surface temperature from Himawari-8. *J Meteorol Soc Jpn* 96B:43–58. <https://doi.org/10.2151/jmsj.2018-004>
- Yang J, Huang X (2021) The 30 m annual land cover dataset and its dynamics in China from 1990 to 2019. *Earth Syst Sci Data* 13:3907–3925. <https://doi.org/10.5194/essd-13-3907-2021>
- Zaitunah A, Samsuri S, Silitonga AF, Syaufina L (2022) Urban greening effect on land surface temperature. *Sensors* 22. <https://doi.org/10.3390/s22114168>
- Zhou D, Xiao J, Bonafoni S, Berger C, Deilami K, Zhou Y, Frolking S, Yao R, Qiao Z, Sobrino JA (2018) Satellite remote sensing of surface urban heat islands: progress, challenges, and perspectives. *Remote Sensing* 11(1):48. <https://doi.org/10.3390/rs11010048>

Publisher's Note Springer Nature remains neutral with regard to jurisdictional claims in published maps and institutional affiliations.

Springer Nature or its licensor (e.g. a society or other partner) holds exclusive rights to this article under a publishing agreement with the author(s) or other rightsholder(s); author self-archiving of the accepted manuscript version of this article is solely governed by the terms of such publishing agreement and applicable law.